

# Accommodative holography: improving accommodation response for perceptually realistic holographic displays

DONGYEON KIM\* and SEUNG-WOO NAM\*, Seoul National University, Republic of Korea  
BYOUNGHYO LEE, Seoul National University, Republic of Korea  
JONG-MO SEO, Seoul National University, Republic of Korea  
BYOUNGHO LEE, Seoul National University, Republic of Korea

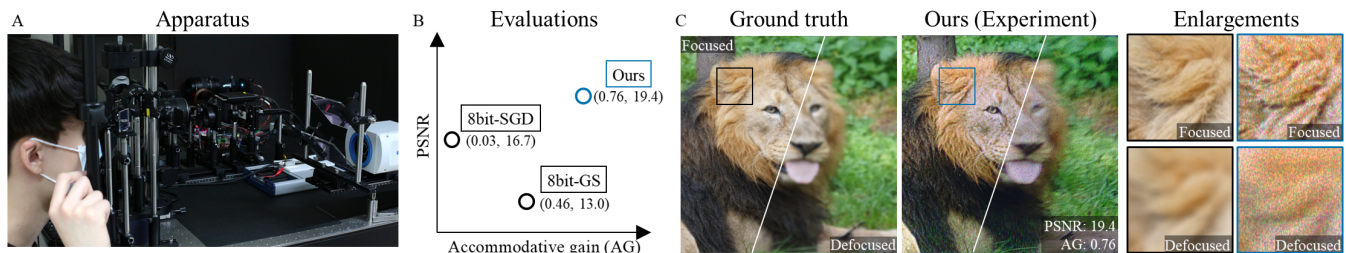


Fig. 1. Holographic display with enhanced accommodation cue. Recently, computer-generated holography (CGH) algorithms are primarily evaluated based on pictorial metrics, such as peak signal-to-noise ratio (PSNR). However, it has become unclear whether holographic displays trigger accommodation response. With the prototype of holographic near-eye display as an (A) experimental apparatus, we (B) evaluate the recently introduced CGH algorithm (8bit stochastic gradient descent (8bit-SGD)) and classical algorithm (8bit Gerchberg-Saxton (8bit-GS)) based on PSNR and accommodative gain (AG) measured with experiments. Furthermore, we introduce potential approaches to improve accommodation response in holographic viewing experiences. The (C) captured results of the introduced approach on hologram acquisition (Ours, blue) with our display prototype show similarities compared to the ground truth case of incoherent display (black) in both focused and defocused images. Through experiments including user studies, we demonstrate that the introduced methods significantly improve accommodative gain with minimal quality degradation, which ultimately contribute to the realization of perceptually realistic holographic displays. Image sources from DIV2K dataset [Agustsson and Timofte, 2017].

Holographic displays have gained unprecedented attention as next-generation virtual and augmented reality applications with recent achievements in the realization of a high-contrast image through computer-generated holograms (CGHs). However, these holograms show a high energy concentration in a limited angular spectrum, whereas the holograms with uniformly distributed angular spectrum suffer from a severe speckle noise in the reconstructed images. In this study, we claim that these two physical phenomena attributed to the existing CGHs significantly limit the support of accommodation cues, which is known as one of the biggest advantages of holographic displays. To support the statement, we analyze and evaluate various CGH algorithms with contrast gradients - a change of contrast over the change of the focal diopter of the eye - simulated based on the optical configuration of the display system and human visual perception models. We first introduce two approaches to improve monocular accommodation response in holographic

viewing experience; optical and computational approaches to provide holographic images with sufficient contrast gradients. We design and conduct user experiments with our prototype of holographic near-eye displays, validating the deficient support of accommodation cues in the existing CGH algorithms and demonstrating the feasibility of the proposed solutions with significant improvements on accommodative gains.

CCS Concepts: • **Hardware** → **Displays and imagers**; *Emerging optical and photonic technologies*; • **Computing methodologies** → **Perception**; *Mixed / augmented reality*.

Additional Key Words and Phrases: holographic display, accommodation, speckle, optimization

## ACM Reference Format:

Dongyeon Kim, Seung-Woo Nam, Byoung-hyo Lee, Jong-Mo Seo, and Byoung-ho Lee. 2022. Accommodative holography: improving accommodation response for perceptually realistic holographic displays. *ACM Trans. Graph.* 41, 4, Article 111 (July 2022), 15 pages. <https://doi.org/10.1145/3528223.3530147>

## 1 INTRODUCTION

As virtual reality experiences and real-world experiences are beginning to converge, the importance of user experience through visual devices is being emphasized. Relieving visual fatigue derived from display devices is essential for sustainable visual experiences; the topic has long been of interest in the computer graphics, optics, and vision science communities. As a candidate of display configuration, holographic display incorporated with computer-generated hologram (CGH) has full potentials to be a next-generation virtual reality (VR) platform owing to the versatile functionalities such

\*Both authors contributed equally to this research.

Authors' addresses: Dongyeon Kim, [dongyeon93@snu.ac.kr](mailto:dongyeon93@snu.ac.kr); Seung-Woo Nam, [711asd@snu.ac.kr](mailto:711asd@snu.ac.kr), Seoul National University, Republic of Korea; Byoung-hyo Lee, [yui145263@gmail.com](mailto:yui145263@gmail.com), Seoul National University, Republic of Korea; Jong-Mo Seo, [callme@snu.ac.kr](mailto:callme@snu.ac.kr), Seoul National University, Republic of Korea; Byoung-ho Lee, [byoung-ho@snu.ac.kr](mailto:byoung-ho@snu.ac.kr), Seoul National University, Republic of Korea.

Permission to make digital or hard copies of all or part of this work for personal or classroom use is granted without fee provided that copies are not made or distributed for profit or commercial advantage and that copies bear this notice and the full citation on the first page. Copyrights for components of this work owned by others than ACM must be honored. Abstracting with credit is permitted. To copy otherwise, or republish, to post on servers or to redistribute to lists, requires prior specific permission and/or a fee. Request permissions from [permissions@acm.org](mailto:permissions@acm.org).

© 2022 Association for Computing Machinery.

0730-0301/2022/7-ART111 \$15.00

<https://doi.org/10.1145/3528223.3530147>

as support of focus cues, provision of high-resolution images, and capabilities in the correction of both visual and optical aberrations. However, a major challenge is the realization of high-quality holographic images with reduced speckle noise inherently present in holographic displays.

Recent state-of-the-art works on holography have begun to visualize a high-quality photorealistic holographic image with less artifacts using computational approaches. Maimone et al. [2017] and Shi et al. [2021] adopted direct encoding methods of the complex-valued hologram with a phase-only spatial light modulator (SLM). Instead of heuristic phase retrieval approaches, Chakravarthula et al. [2019] proposed a high-fidelity phase retrieval framework with first-order optimization that can be employed in various optimization problems. Furthermore, Peng et al. [2020] and Chakravarthula et al. [2020] proposed with algorithmic hologram acquisition frameworks that bridge the gap between ideal and physical wave propagation by exploiting the differentiable physical model proxy accessed by capture devices. These works presented a high-contrast and speckle-reduced holographic image. However, the observed images exhibit relatively small blurs compared to the classical holographic images (e.g., Gerchberg-Saxton algorithm [Gerchberg, 1972]) containing speckle noise, when they are optically defocused. Therefore, it can be carefully inferred that these holograms may not exhibit a major advantage of holographic displays: the monocular accommodation cue.

However, it has neither been thoroughly investigated whether holographic displays properly trigger monocular accommodation response, nor has it been validated with user experiments. Takaki and Yokouchi [2012], and Ohara et al. [2015] measured static accommodation responses on their table-top holographic displays. In these studies, the vergence cue was not eliminated as the images were provided to both eyes, although the measured diopter when viewing a holographic stimulus was in accordance with that measured when seeing a real-world scene. Furthermore, for a monocular eye, Nozaki et al. [2017] failed to demonstrate that the holographic stimulus is similar to the real target in eliciting accommodation response, although the reconstructed images were free of speckle noise with light-emitting diode (LED) illumination. Therefore, none of the works performed so far have confirmed whether a holographic display can elicit an appropriate monocular accommodation response or identified the potential factors limiting or enhancing accommodation response.

In this work, we address the unexplored topic on holographic displays, investigate prerequisite conditions of CGHs to properly trigger monocular accommodation, and conceive approaches to improve the response to ultimately pursue perceptual realism with holographic displays. Considering the optical configuration of the display system and the human visual perception models to validate their support of monocular accommodation cues, we simulate the contrast gradients - change of the contrast over the change of the focal diopter of the eye - of holographic contents acquired with various CGH algorithms. We design and conduct user studies to experimentally measure user data for the evaluations. Specifically, we

quantitatively measure accommodation response and assess the subjective image quality of the holographic contents with pairwise comparisons. The evaluations are performed on our prototypes of holographic near-eye displays. We confirm that the holographic near-eye display with existing CGHs rarely or weakly induces monocular accommodation response, and our approaches significantly improve the accommodative gain with an indistinguishable degradation in subjective image quality.

The contributions of this study are as follows.

- We question whether the holographic near-eye displays with existing CGHs trigger sufficient monocular accommodation response by simulating a contrast curve of the holographic images based on the optical model of the display system and the human visual perception models.
- We introduce two approaches to improve accommodative gain in holographic VR experiences; an optical solution of speckle reduction (not technically novel), that presents multiple hologram frames within the flicker threshold of an eye, and a computational solution that provides CGHs optimized with regularization on contrast ratio, to deliver holographic stimuli with sufficient contrast gradients.
- We design and conduct user studies with prototypes of holographic near-eye displays to evaluate the introduced approaches, demonstrating the significances of accommodative gain improvement with indistinguishable subjective image quality degradation.

## 2 RELATED WORKS

### 2.1 Human vision

**2.1.1 Depth perception.** Humans perceive depth information through a combination of oculomotor movements and several visual cues. Vergence and accommodation exist in oculomotor movements. Vergence is an eye rotation motion that fuses images seen through both eyes sharply, and inaccurate vergence results in double vision of the fixated object. Accommodation is the focal power adjustment of the eye lens to obtain a sharp image with one eye. Incorrect accommodation of the eye lens causes blurs in the retinal image. These two oculomotor motions demonstrate a neural coupling [Cumming and Judge, 1986, Martens and Ogle, 1959], and each response acts as a factor that triggers the other. However, vergence is primarily induced by retinal disparity, while accommodation is mainly triggered by retinal blur.

Retinal blur, as a visual cue to trigger accommodation, is directly affected by aberration and pupil size of the eye. Among eye aberrations, which vary among individuals, monochromatic aberrations, such as defocus and astigmatism can impede accommodation response. Whereas the intrinsic presence of chromatic aberration in the human eye can positively trigger accommodation [Fincham, 1951, Kruger et al., 1993]. Furthermore, the eye pupil that manages the influx of light by modulating its size can change aberration, diffraction, and depth of focus which further influences the accommodation response. Additionally, there are psychological factors such as texture gradient, object overlapping, shadowing, and motion-based factors, such as motion parallax that affect monocular accommodation [Reichelt et al., 2010].

**2.1.2 Image perception.** The image perception through the human visual system is constrained in space and time domains. First, the spatial sensitivity is primarily affected by the optical transfer function of the eye, governed by several factors such as pupil size [Watson, 2013], lens aberration [Thibos et al., 2002], and retinal eccentricity [Navarro et al., 1993]. Furthermore, the neural transfer function describes additional modulators generated by the retina-brain systems [Banks et al., 1987]. Thus, the spatial contrast sensitivity function, which encompasses the impact of the overall factors, describes the spatial resolution of the human visual system [Barten, 1999, Daly, 1992, Kelly, 1979]. The highest spatial frequency that the human eye can perceive is known as approximately 48 cycles per degree (cpd) [Guenter et al., 2012] in the fovea region and conservatively 30 cpd. Similarly, the temporal sensitivity of the human visual system is measured with a visual stimulus with different temporal frequencies in various luminance levels [Tyler and Hamer, 1990]. The temporal resolution, which is equal to the critical flicker fusion threshold, is approximately 50 Hz when a target with low luminance and low spatial frequency is projected on the near-fovea region [Krajancich et al., 2021]. Humans perceive the superimposed intensity profile when a visual stimulus is updated faster than the temporal threshold.

## 2.2 Holography

Holography is a technology that records wavefronts through interference between two coherent beams and reproduces the wavefronts with reference beam illumination afterward. Benton and Bove [2008] introduced a holographic video based on computer-generated holography using laser, spatial light modulator, and computer. The spatial light modulator (SLM) reconstructs the wave field with the CGH obtained through the complex wavefront numerically calculated based on wave diffraction theory and the pattern encoding algorithms. Because the theory on wave propagation [Goodman, 2005] has been established beyond a certain level, several studies have focused on CGH acquisition to desirably reconstruct the complex-valued field despite the existence of physical constraints. The modulated physical quantity and the bit depth of SLM are determined based on the optical configuration and operating characteristics of the SLM.

Phase modulation with SLM is achieved using liquid crystals that provide per-pixel phase delay of the incident polarized beam. For the phase-only CGHs, the amplitude discard method is the simplest solution as it directly extracts the phase component in the complex-valued field. However, the reconstructed image contains noticeable artifacts as it ignores the amplitude component. Another straightforward solution is double phase-amplitude encoding [Hsueh and Sawchuk, 1978, Lee, 1970, Maimone et al., 2017, Shi et al., 2021], in which a pair of adjacent pixels of SLM represents a single complex value. In addition to the direct phase retrieval strategies, several iterative methods acquire a phase pattern with optimization to present better image quality [Chakravarthula et al., 2019, 2020, Fienup, 1982, Gerchberg, 1972, Peng et al., 2020]. Conversely, amplitude modulating SLMs, generally realized with micromirrors [Lee et al., 2020c, Takaki and Okada, 2009] or ferroelectric liquid crystals [Broomfield et al., 1992], are often encoded based on binarized amplitude. The incomplete representation of complex-valued fields only with the binarized amplitude causes a low signal-to-noise ratio (SNR) in

the reconstructed holographic image. Rapid operation speed is a powerful advantage of the binary SLMs compared to the existing 8bit SLMs. Recently, works on binary amplitude CGH optimization with the stochastic gradient descent method have been conducted to mitigate the SNR degradation. [Curtis et al., 2021, Lee et al., 2022]

Other than the operation scheme of SLM, the coherent characteristics of the light source influence the quality of the reconstructed holographic images [Deng and Chu, 2017]. For example, a holographic display realized with a laser demonstrates sharp holographic images but suffer from severe speckle noise [Goodman, 2007] due to randomized interference of coherent field. Conversely, partially coherent light sources such as light-emitting diodes reconstruct speckle-reduced images; however, a proportional loss of image resolution appears. Overall resolution degradation depends on the aperture size of the light source, the light spectrum, and the reconstruction distance from the SLM. Considering these aspects, the light source of the holographic display can be customized depending on the display configuration [Lee et al., 2020b]. Furthermore, recent work on holographic display with a partially coherent light source bypassed the resolution loss problem with the camera-in-the-loop calibration [Peng et al., 2021].

As a display system, holographic displays have been implemented in a form of table-top displays [Lim et al., 2016, Park et al., 2019], projector [Wakunami et al., 2016] and near-eye displays [Jang et al., 2018, Maimone et al., 2017]. In particular, holographic near-eye displays have been recently highlighted as virtual and augmented reality applications with versatile functionalities such as support of focus cues [Chang et al., 2020], aberration, and vision correction [Kim et al., 2021]. A near-eye display is realized by placing an additional lens which converges the reconstructed holographic image into the eye. Studies on holographic near-eye displays have mainly focused on improving the physical specifications of the display by miniaturization using diffractive optics [Li et al., 2016, Maimone et al., 2017, Yeom et al., 2015], eye-box expansion with a steering device [Jang et al., 2018], and field of view enlargement using a micro-structured mask [Kuo et al., 2020]. Unlike other advanced displaying schemes, such as multi-plane displays [Akeley et al., 2004, Lee et al., 2019, Ravikumar et al., 2011], light field displays [Huang et al., 2015, Jang et al., 2017, Wetzstein et al., 2012], and gaze-contingent displays [Konrad et al., 2017, Padmanaban et al., 2017], no study has focused on improving the visual experience of holographic near-eye displays.

## 3 MOTIVATION

Accommodation response is primarily driven by retinal blur that changes depending on the focal states. Therefore, we simulated holographic images (Fig. 2) acquired with two representative iterative CGH algorithms (Stochastic Gradient Descent (SGD) [Peng et al., 2020] and Gerchberg-Saxton (GS) [Gerchberg, 1972]) as shown in Fig. 2(A). The SGD hologram delivers a high-contrast holographic image like ground truth in the focused state, while the defocused image shows a slight blur compared to the ground truth case of an incoherent display. However, in image presented by the GS hologram, the image defocused with the difference of 0.6 diopter (D),

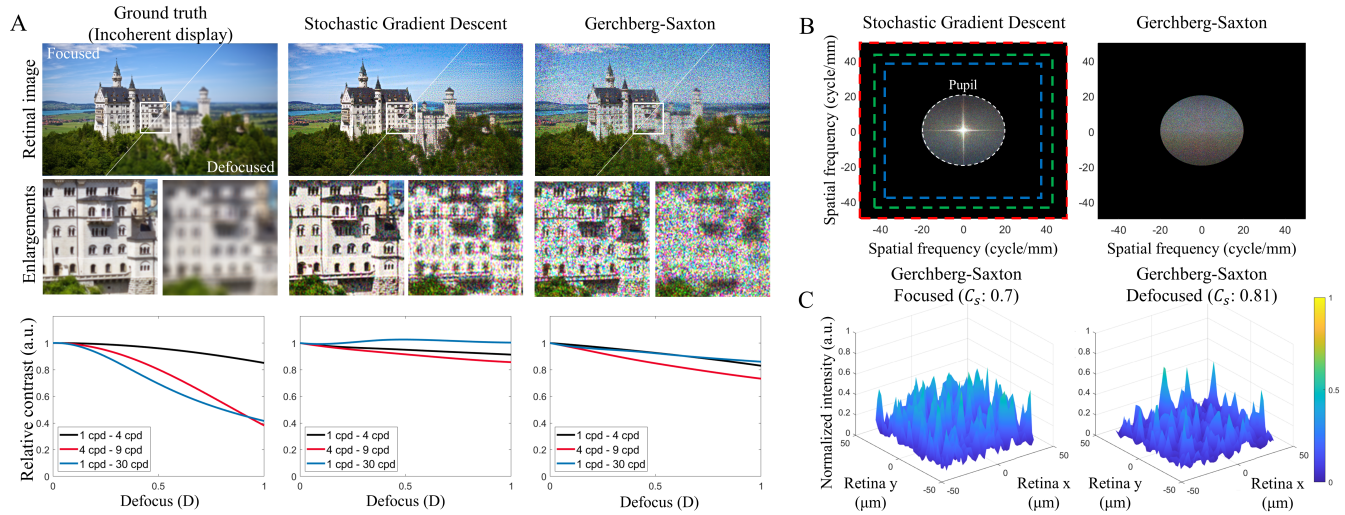


Fig. 2. Reconstructed holographic images of representative CGH algorithms in simulation. (A) The retinal images of three display schemes (an incoherent display as ground truth, holographic displays with phase-only CGHs acquired with stochastic gradient descent (SGD) algorithm [Peng et al., 2020], and Gerchberg-Saxton algorithm [Gerchberg, 1972]) reconstructed at the focused state. The defocused state with the dioptric error of 0.6 D are provided with additional enlarged views. The contrast curves of each scheme are provided in the bottom row describing the different spatial frequency regions (1-4 cpd (black), 4-9 cpd (red), and 1-30 cpd (blue)). (B) The magnitudes of the angular spectrum of the field reconstructed under identical conditions and processed to represent the same mean and threshold are provided with dashed lines indicating the bandwidths of each color primaries (red, green, and blue), and the area corresponding to the pupil (white) with a diameter of 3 mm. The reconstructed images with SGD holograms demonstrate slight contrast gradients because of the narrow size of effective bandwidth. However, in the case of GS holograms, (C) speckle noise present in both focused image (left) and defocused image (right) with speckle contrast of 0.7 and 0.81, respectively, may limit the contrast gradient, although it showed relatively uniform angular spectrum. Here, speckle contrast ( $C_s$ ) is estimated as a ratio of the standard deviation of the reconstructed intensity over the mean intensity.

reciprocal of the metric focal length) looks sufficiently blurry, but the speckle noise is severe in the focused and defocused images.

Neither of the cases exhibit a contrast curve similar to the contrast curve simulated with the ground truth case of an incoherent display as shown in the bottom row of Fig. 2(A). Specifically, the contrast ratio of the regions that correspond to the middle spatial frequency range (4-9 cpd) or broadband stimulus (1-30 cpd) varies noticeably from the ground truth case. The potential causes underlying this phenomenon may differ for each case: a narrow size of effective bandwidth for the SGD hologram case (Fig. 2(B)) and the existence of speckle noise in both focused and defocused images for the GS holograms (Fig. 2(C)). In this study, we assume that the holograms processed with two algorithms (SGD and GS) represent each physical cause, although there may be other CGH algorithms with quality improvement.

#### 4 ACCOMMODATIVE HOLOGRAPHIC NEAR-EYE DISPLAY

Our primary goal is to assess the holographic contents acquired with the conventional CGH algorithms in terms of contrast gradient and solve the limited contrast gradient problem that further results in inadequate accommodation response. Prior to the evaluations, we formulate the wave propagation model utilized in both acquisition of CGH and reconstruction of a holographic image. Subsequently, the contrast curves of each display scheme are simulated under the optical specifications of the near-eye display prototypes built

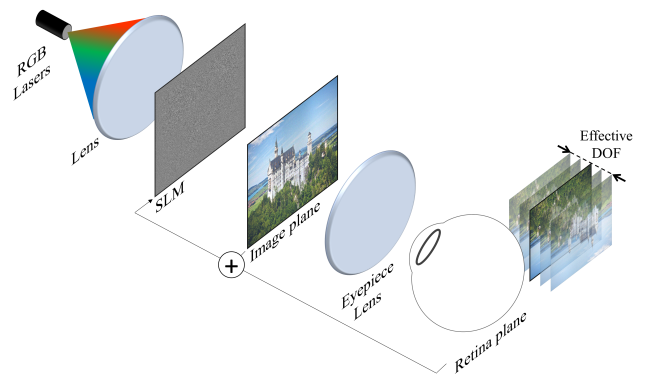


Fig. 3. Illustration of Fresnel-type holographic near-eye display configuration. A full-color holographic image realized by RGB lasers, SLM, and CGHs is provided in the image plane. Subsequently, the image is projected to the viewer's retina plane. This work aims to narrow the effective depth of focus (DOF) of the projected holographic stimulus similar to that of an incoherent stimulus to trigger accommodation response through holographic displays similar to real-world viewing experience.

for the evaluation. Finally, we introduce potential approaches that resolve the limited contrast gradient problem in existing holographic contents.

#### 4.1 Holographic wave propagation

In a Fresnel-type holographic near-eye display configuration, the coherent laser beam collimated with a lens is incident on the SLM that either modulates the amplitude or the phase component to represent the complex field  $z = ae^{i\phi} \in \mathbb{C}^{M \times N \times 3}$  as shown in Fig. 3. The field distribution in the plane apart from the SLM can be numerically calculated with the wave diffraction theory. Among the wave propagation models, angular spectrum method [Goodman, 2005] is widely used, and the propagated field can be represented with this model as

$$\mathcal{P}_d(g(z)) = \iint \mathcal{F}(g(z)) \mathcal{H}(v_x, v_y; d, \lambda) e^{i2\pi(v_x x + v_y y)} dv_x dv_y, \quad (1)$$

$$\mathcal{H}(v_x, v_y; d, \lambda) = \begin{cases} e^{i\frac{2\pi d}{\lambda} \sqrt{1 - (\lambda v_x)^2 - (\lambda v_y)^2}}, & \text{if } \sqrt{v_x^2 + v_y^2} < \frac{1}{\lambda}, \\ 0, & \text{otherwise} \end{cases}$$

where,  $x, y$  are coordinates of SLM domain,  $\mathcal{P}_d(\cdot)$  is a propagation operator with a distance of  $d$ ,  $\mathcal{F}(\cdot)$  is the two-dimensional Fourier transform operator,  $g(\cdot)$  is the SLM decoding operator,  $\lambda$  is the wavelength of the laser beam,  $v_x, v_y$  are the spatial frequencies and  $\mathcal{H}(\cdot)$  is the transfer function.

The decoding operator varies in its form depending on the modulating scheme of SLMs. For the SLMs with phase-only modulation, we consider the amplitude as a constant, and the field is expressed as  $g(z) = e^{i\phi}$ . For the amplitude-type SLMs, the target field is paired with its complex conjugate as  $g(z) = \text{real}(z) = \frac{ae^{i\phi} + ae^{-i\phi}}{2}$ . The complex conjugate of the target complex field can be eliminated by off-axis type CGHs and optical redirection of the reference beam. For binary amplitude SLMs, additional binarization is performed and the operator is expressed as  $g(z) = \text{sign}(\text{real}(z))$ .

The acquisition of the complex-valued hologram is usually performed by solving the minimization problem formulated in the amplitude basis as follows:

$$\underset{z}{\text{minimize}} \mathcal{L}(s \cdot |\mathcal{P}_d(g(z))|, a_{\text{target}}). \quad (2)$$

Here,  $s$  is a scale factor that balances the overall value difference between  $|\mathcal{P}_d(g(z))|$  and  $a_{\text{target}}$ . For acquisition of a phase pattern, the optimization variable is down-streamed into the real value presented as  $\phi \in \mathbb{R}^{M \times N \times 3}$ . The loss function ( $\mathcal{L}$ ) is generally in the form of  $l_1$  or  $l_2$  error and the solution of these problems can be acquired using first-order gradients as recently introduced by Peng et al. [2020] adopting SGD solver.

#### 4.2 Contrast ratio of visual stimulus

Assuming that the complex field distribution of  $u \in \mathbb{C}^{M \times N \times 3}$  is reconstructed at the focal length ( $f_{EL}$ ) of an eyepiece lens, and an eye with the dioptric error of  $\Delta D$  is positioned at the opposite focal plane of the eyepiece. The amplitude transfer function characterizes the optical relation defined in coherent imaging system is obtained as follows.

$$ATF_{\Delta D}(v_x, v_y) = \mathcal{A}(f_{EL} v_x, f_{EL} v_y) e^{i\frac{2\pi}{\lambda} \mathcal{W}_{\Delta D}(f_{EL} v_x, f_{EL} v_y)} \quad (3)$$

where,  $\mathcal{A}$  is the apodization function, and  $\mathcal{W}_{\Delta D}$  is the aberration function of the given system with additional eye dioptric error of  $\Delta D$ .

If the eye pupil is diffraction-limited and circular with a radius of  $r_{ep}$ , it functions as a finite passband in the frequency domain and corresponding apodization function are represented as  $\mathcal{A} = \text{circ}\left(\frac{f_{EL} \sqrt{v_x^2 + v_y^2}}{r_{ep}}\right)$ . Similarly, the aberration function, which is caused by the path-length error of the beam incident to the pupil, is expressed in a quadratic form of spatial frequencies as  $\mathcal{W}_{\Delta D} = f_{EL}^2 \pi \Delta D (v_x^2 + v_y^2) / \lambda$ . In a coherent optical system, the intensity profile of the plane optically conjugates to the retinal plane is an absolute square of the reconstructed field as

$$I_{c,\Delta D}(u) = \left| \mathcal{F}^{-1}(\mathcal{F}(u) ATF_{\Delta D}(v_x, v_y)) \right|^2, \quad (4)$$

where,  $\mathcal{F}^{-1}(\cdot)$  is a two-dimensional inverse Fourier transform. The processed image is resized to a lower resolution to simulate the projected image in the retinal plane with a unit cell of  $2 \mu\text{m} \times 2 \mu\text{m}$ .

Humans do not sense the visual stimulus directly; therefore, we make perceptually plausible assumptions to simulate the perceived image. We obtain the perceived image by multiplying frequency-dependent weight corresponding to the contrast sensitivity function (CSF) to the frequency components of the retinal image reconstructed under the diffraction-limited condition since the CSF approximates a high-level visual function. The contrast ratio, which is a ratio of the perceived image with a dioptric error over the focused image, is represented depending on each spatial frequency band  $\mathcal{S} : [v_{\text{min}}, v_{\text{max}}]$  as

$$CR_{\mathcal{S}}(I_{\Delta D}) = \frac{\iint_{\mathcal{S}} \mathcal{F}(I_{\Delta D}) \text{CSF}(v_x, v_y) dv_x dv_y}{\iint_{\mathcal{S}} \mathcal{F}(I_0) \text{CSF}(v_x, v_y) dv_x dv_y}. \quad (5)$$

We apply the CSF model investigated by Barten [1999] because the model is additionally parameterized with the background luminance level. Luminance condition of conventional VR device, HTC vive pro with the reported luminance level of  $133.3 \text{ cd/m}^2$  [Mehrfard et al., 2019] and the background brightness level of  $0.1 \text{ cd/m}^2$  are adopted to determine the CSF. Additionally, we assume that CSF is constant over the retinal eccentricity because the display prototype provides an image with a limited field of view. Through out the paper, contrast gradient refers to the change of contrast ratio over the change in the focal diopter of the eye.

Similarly, when the incoherent image  $i \in \mathbb{R}^{M \times N \times 3}$  is present in the optically equivalent condition, the reconstructed image defined in the incoherent optical system is presented as

$$I_{i,\Delta D}(i) = \mathcal{F}^{-1}(\mathcal{F}(i) (ATF_{\Delta D}(v_x, v_y) \star ATF_{\Delta D}(v_x, v_y))), \quad (6)$$

where, the symbol  $\star$  denotes the autocorrelation integral. The contrast ratio of the incoherent stimulus is estimated by substituting the intensity term in Eq. 5 with Eq. 6. An incoherent visual stimulus is considered ground truth case similar to the real-world scenes.

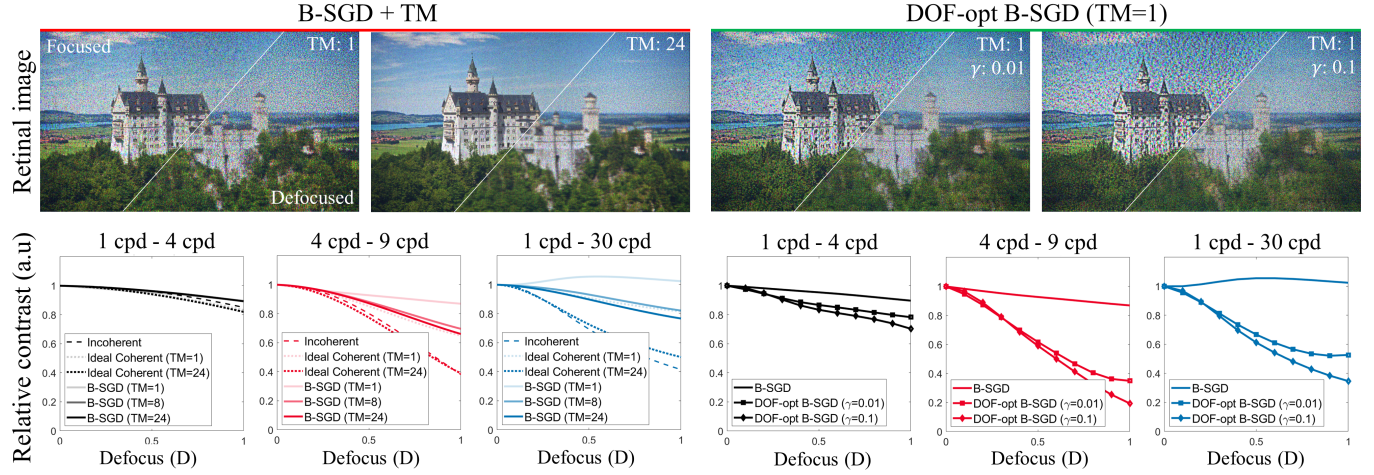


Fig. 4. Holographic contents and corresponding contrast curves obtained through simulation. Reconstructed retinal images of different holographic contents (B-SGD (red), and DOF-opt B-SGD (green)) in both focused and defocused states are provided in the first row with the stated TM conditions on each image. The contrast curves of the reconstructed holographic images are provided in different colors indicating the specific range of spatial frequency (first col: 1-4 cpd (black), second col: 4-9 cpd (red), third col: 1-30 cpd (blue)). *Incoherent*, *Ideal Coherent*, B-SGD, DOF-opt B-SGD ( $\gamma=0.01$ ), and DOF-opt B-SGD ( $\gamma=0.1$ ) correspond to dashed line, dotted line, solid lines without a marker, with a square marker, and a diamond marker, respectively. The transparencies of individual lines are adjusted based on the TM conditions. The demonstrated images are reconstructed under conditions of pupil diameter of 3 mm and eye-box of 5.27 mm  $\times$  2.64 mm. Image sources from DIV2K dataset [Agustsson and Timofte, 2017].

### 4.3 Accommodative holography

In this subsection, we introduce two approaches for a holographic display to improve accommodation response by providing holographic stimuli with sufficient contrast gradients as incoherent stimuli. The first approach is speckle noise reduction in the realized holographic image. We adopt an optical solution known as temporal multiplexing as a practical approach. The next approach is providing CGHs optimized with a regularization strategy to realize holographic images with manipulated contrast ratio to smoothly guide accommodation, although the speckle is present in the holographic images.

**4.3.1 Speckle reduction through temporal multiplexing.** The intensity profile realized with temporal multiplexing (TM) of the holograms can be described as an average of the reconstructed intensity profiles defined in linear color space as

$$I_{TM} = \frac{1}{J} \sum_{j=1}^J I_c (s \cdot \mathcal{P}_d (g(z_j))), \quad (7)$$

where,  $J$  is the number of holograms acquired with the different orthogonal random distribution of phase. The scale factor is set to be constant within the TM frames. Notably, the speckle contrast, which is the standard deviation of the intensity over the mean intensity, decreases proportionally to the square root of the number of frames exploited in TM [Lee et al., 2020c]. The TM technique optically reduces the speckle noise without a loss of spatial resolution. However, in practice, it can only be realized with binary SLMs with a rapid operation speed. Thus, we adopt the recent work on binary hologram optimization with stochastic gradient descent algorithm (B-SGD) [Lee et al., 2022] as a means to implement the

holographic TM and visualize a holographic image with a minimal contrast degradation derived from the additional binarization. We revised the CGH acquisition algorithm to obtain Fresnel-type binary hologram described in Supplementary Material.

Figure 4 demonstrates the reconstructed holographic images and corresponding contrast curves. The TM of the holograms reduces the speckle noise presented in both in-focus and out-of-focus images as shown in the two images placed in the left section of Fig. 4. The contrast curves of the reconstructed images of two different schemes (*Ideal Coherent*, B-SGD) are provided with different TM conditions with a ground truth case of incoherent display (*Incoherent*) as shown in the second row of Fig. 4. Here, we dub *Ideal Coherent* when a complex-valued field with random phase distribution is reconstructed without additional procedures affecting the original field such as encoding and propagation. The contrast curves of *Ideal Coherent* are similar to those of *Incoherent* when the speckle noise is reduced with TM. The contrast curves of the images acquired with B-SGD holograms are also shown with different TM conditions. Although the contrast curves are dissimilar to the ideal cases, speckle reduction through TM effectively degrades the contrast in the defocused image, especially in the middle spatial frequency region (4-9 cpd) and the broadband range (1-30 cpd).

**4.3.2 CGH optimization with contrast ratio regularization.** Suppressing the speckle noise through TM is an effective method for smoothly degrading contrast over the focal states. However, it is often burdensome as the hologram acquisition time increases proportionally to the number of frames required for TM. Therefore, in this subsection, we introduce a CGH optimization strategy to effectively design the contrast ratio of the holographic stimulus with a minimal quality degradation in the focused image. Specifically, the loss function

consists of the mean squared error between the reconstructed and target amplitude and the regularization term on contrast ratio as

$$\begin{aligned} \mathcal{L}_{ours} = \mathcal{L}_a + \mathcal{L}_{CR} = & \|s \cdot |\mathcal{P}_d(g(z))| - a_{target}\|_2^2 \\ & + \frac{\gamma}{N} \sum_{n=1}^N \|CR_S(\Gamma(I_{c,\Delta D_n}(s \cdot \mathcal{P}_d(g(z)))))) - CR_{S,\Delta D_n,target}\|_1 \end{aligned} \quad (8)$$

where,  $\|\cdot\|_1$ ,  $\|\cdot\|_2$  represent  $l_1$  and  $l_2$  norm operators, respectively,  $\gamma$  is a user-defined regularization coefficient that balances the two loss terms,  $N$  is the total number of focal states considered in the optimization procedure, and  $\Gamma(\cdot)$  is the sRGB gamma correction operator which is approximately  $(\cdot)^{1/2.2}$ .

The amplitude loss ( $\mathcal{L}_a$ ) is a square of  $l_2$  norm of the difference between the reconstructed and target amplitude. In the regularization term, the contrast ratio loss ( $\mathcal{L}_{CR}$ ) is defined as the average of  $l_1$  norm of difference between the contrast ratio of the reconstructed holographic image and that of incoherent stimulus estimated at each focal state. Here,  $a_{target} = \sqrt{i_{lin}} = (\Gamma^{-1}(i))^{1/2} \approx i$  is the target amplitude for CGH optimization which is approximately the target image in sRGB color space, and  $CR_{S,target,\Delta D_n} = CR_S(I_{i,\Delta D_n}(i))$  is the target contrast ratio acquired with the incoherent image. The contrast ratio is estimated in a spatial frequency band ranging from 1-30 cpd. The CGH acquisition by reducing the linear combination of  $l_1$  and  $l_2$  norm based on multi-plane reconstruction has recently been proposed [Choi et al., 2021]. Their aim is to reconstruct a 3-D holographic scene with a piecewise smoothed phase profile and ours is to minimize the contrast ratio loss. Adoption of their method in acquisition of CGH reconstructing a 2-D holographic image does not differ much compared to the visualization of SGD CGH in terms of the effective size of eye-box and the resultant defocused images. The simulation results are provided in Supplementary Material.

The optimization with additional regularization term results in quality degradation in the focused image as shown in the reconstructed images presented in the right section of first row of Fig. 4. The problem weighs more in the latter loss as the regularization coefficient gets larger, which results in an image with more artifacts. The contrast curves of the corresponding holographic images are provided with the case of B-SGD hologram in the second row of Fig. 4. The optimized hologram with a large regularization coefficient ( $\gamma=0.1$ ) exhibited a contrast curve of broadband frequency range (1-30 cpd) similar to that of the ground truth case. However, the contrast curve of the DOF-opt B-SGD ( $\gamma=0.01$ ) stimulus at the middle spatial frequency region (4-9 cpd) is close to the incoherent case compared to the DOF-opt B-SGD ( $\gamma=0.1$ ). Accommodation and blur perception are primarily driven by the spatial frequency ranging from 4-9 cpd [Mathews and Kruger, 1994, Owens, 1980].

## 5 IMPLEMENTATION

In this section, we explain the implementation of the work which is broadly categorized into two: hardware and software. We put in substantial efforts to implement the entire system suitable for off-line user experiments (Sec. 6-7). Prior to user experiments, we provide the captured holographic scenes.

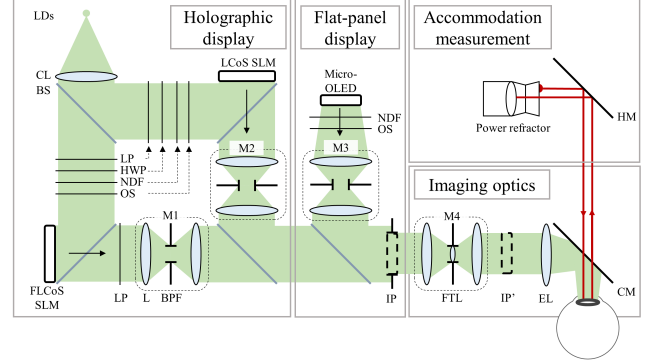


Fig. 5. Schematic of the apparatus built for the experimental assessments. The individual displays head to the directions indicated by black arrows, and the beams share a single optical path with the focus-tunable lens placed to tune the axial distance of the image. Given an image, the power refractor measures the eye's refractive power in infrared light, the path of which is indicated by a red line. Some optical components or devices are omitted in this illustration for simplicity. The photograph of the entire system can be found in the Supplementary Material.

### 5.1 Hardware

Figure 5 presents the schematic of the apparatus utilized in the experimental assessments. The entire system can be categorized into four parts: Fresnel-type holographic displays with two different SLMs, a flat-panel display, accommodation measurement devices, and other imaging optics.

First, for the holographic display section, the laser source utilized in the hardware setup is a fiber-coupled laser diode (LD) of Wikiopics, which emits a full-color beam with the central wavelengths 638, 520, and 450 nm. Full-color holographic visualization is conducted by synchronizing the color sequence with the SLMs. The beam collimated with a lens is split into two beam paths using a beam splitter (BS) while we exploit two different spatial light modulators for the assessment. One of the split beams passes through a series of a linear polarizer (LP) and a half-wave plate (HWP) to match the polarization angle of the beam with that required by ferroelectric liquid crystal on silicon spatial light modulator (FLCoS SLM). Additionally, a neutral density filter (NDF) and an optical shutter (OS) are additionally placed in the middle of the optical path to attenuate and block the beam, respectively. The FLCoS SLM, a product of Fourth Dimension Displays, with a pixel pitch of  $8.2 \mu\text{m} \times 8.2 \mu\text{m}$ , and a resolution of  $1920 \times 1200$ , provides 24 different full-color binary patterns in 50 Hz and modulates the binary amplitude of the field with additional LP placed after the SLM. The FLCoS SLM plane is optically shifted using relay optics built with two camera lenses with a magnification ratio (M1) of 0.78. A bandpass filter (BPF) is placed at the Fourier plane to block the high-order signals. Moreover, the physical size of BPF is determined based on the bandwidth of the blue signal and vertically halved because of the complex encoding of amplitude hologram. Similarly, the other optical path of the laser beam passes through a series of LP, HWP, NDF, and OS, which are placed for identical purposes. The Holoeye LETO LCoS SLM with a pixel pitch of  $6.4 \mu\text{m} \times 6.4 \mu\text{m}$ , a resolution of  $1920 \times 1080$ , and a full-color

operation frame rate of 60 Hz, modulates phase components with a bit depth of eight. The modulated beam passes through a  $4-f$  system ( $M2=1$ ) and a BPF. Both SLMs are provided with the hologram to reconstruct the desired intensity in the target image plane (IP). Both SLMs are vertically rotated at an angle corresponding to half of the diffraction angle of the blue signal to prevent the undiffracted DC noise from entering the eye. The CGHs are processed with an additional shift in the frequency domain for off-axis reconstruction.

A flat-panel display is integrated to measure the accommodative response when viewing the incoherent display and serve the measured value as a reference. A 0.39-inch organic light-emitting diode display (micro-OLED) with FHD ( $1920 \times 1080$ ) resolution, is attenuated by NDF and managed by an OS. The display is optically relayed to the IP with a magnification ratio ( $M3$ ) of 1.5. Notably, the sizes of individual BPFs are determined to match the eye-box size of individual display configurations. The IP is optically relayed by a  $4-f$  system ( $M4=1$ ). A focus-tunable lens (FTL, Optotune EL-16-40-TC-VIS-5D-C) with a clear aperture of 16 mm is placed at the Fourier plane of the optics to tune the axial placement of relayed image plane (IP'). Finally, a 2-inch eyepiece lens with a focal length of 75 mm virtually floats the image located at the IP' to visualize the display scenes. As the eye focuses on the depth-varying display scene, the accommodation response is dynamically measured by the power refractor of Plusoptix (Powerref 3) placed 1 m from the eye. The infrared light emitted by the device is projected into the eye, and the image reflected from the retina is captured by its sensor. The refractive power of the eye is measured at a speed of 50 Hz when the pupil size ranges from 4 to 8 mm. We consecutively placed a hot mirror (HM) and a cold mirror (CM) to prevent the visible light noise from interfering with the information captured with infrared light. See Supplementary Material for the details on system implementation.

## 5.2 Software

We implemented the CGH acquisition using PyTorch. We formulated the forward propagation model, and the PyTorch's automatic differentiation allowed the CGH optimization by monitoring the gradient flow. We used a learning rate of 0.1 for updating the gradient of loss function. The implementation was conducted using a graphic card of Nvidia Geforce RTX 3080 Ti with 12 GB RAM. The iteration of 500 took approximately 20 s to acquire a single hologram frame for the iterative CGH algorithms (GS, SGD, B-SGD) constructed with a plane-to-plane model. However, the optimization with the contrast ratio simulated with ten defocused images and a focused image (from -1.0 to 1.0 D with a unit step of 0.2 D) took 10 min for 500 iterations. Further improvements in the computational speed through parameter tuning and code optimization can be performed. However, the slow computation does not affect the significance of the study.

## 5.3 Experimental Assessment

Prior to user evaluations on holographic contents, we assessed our display prototypes. We captured the individual images of various CGH algorithms with a charge-coupled device (FLIR, GS3-U3-91S6C) that has a resolution of  $3376 \times 2704$  and a pitch of  $3.69 \mu\text{m}$  placed

at the IP without an additional attached lens, as shown Fig. 6. The image is provided 130 mm from the relayed LCoS SLM plane and 200 mm from the relayed plane of FLCoS SLM. The dioptric difference of 0.6 D (1.0-1.6 D) is converted to the metric distance of 2.8 mm in the condition of our near-eye display prototype, where we captured the defocused results. The results of 8bit-SGD exhibited the highest PSNR among the images realized by single-frame CGHs, although they were not sufficiently blurred in the defocused state. The artifacts due to pupil apodization were eliminated as we captured holographic images at the image plane. Additional captured results are provided in Fig. S2-S4 in the Supplementary Material.

## 6 ACCOMMODATION EXPERIMENTS

In this section, we evaluate the various CGH algorithms with user experiments by measuring the accommodation responses to validate the deficient support of accommodation cue in existing CGH algorithms and demonstrate the efficacy of the proposed approaches.

### 6.1 Methods

**6.1.1 Subjects.** Thirty naïve subjects (20–30 years, mean age of 24.2 years) participated in the experiments. Among the participants, 18 were female and the others were male. We recruited the participants with normal or corrected-to-normal acuity and age under 40 because the visual acuity, and the age affect depth of focus and accommodation range, respectively, influencing the overall accommodative gain. Before the tests, the spherical equivalents (SEs) of both eyes of the participants were measured with the autorefractor (Huvitz, HRK-8000A) and the participants were encouraged to participate in the experiment with the eye with a smaller SE. All the participants had normal or corrected-to-normal acuity with the average SE of -0.52 D as provided in Supplementary Information, and none of them reported color deficiency or color-blind vision. The studies adhered to the Declaration of Helsinki. All the subjects gave voluntary written and informed consent. The Institutional Review Board at host institution approved the research.

**6.1.2 Apparatus.** Figure 7 summarizes the entire accommodation experiments. Figure 7(A) demonstrates the apparatus of experimental setup where the participant views a depth-varying two-dimensional (2-D) stimulus with an eye as described in Fig. 7(B). The holographic near-eye display prototype provides the image with a resolution of  $1600 \times 900$ , and the corresponding field of view is  $7.8^\circ \times 4.4^\circ$  with a 2-inch EL with a focal length of 75 mm. The eye-box size of the near-eye display system is provided as  $5.27 \text{ mm} \times 2.64 \text{ mm}$ . Note that the use of ELs with a short focal length increases the field of view but reduces the size of the eye-box, making the holographic near-eye display system optically unsuitable for evaluating accommodative response. The Nyquist frequency of the holographic image is estimated as 102 cpd, which exceeds the maximum spatial resolution that the human eye can perceive [Guenther et al., 2012]. The experiments are conducted with full-color images because the color serves as one of the accommodation cues [Cholewiak et al., 2017, Kruger et al., 1993]. The room was kept sufficiently dark during the tests, except for the stimuli provided by the display prototype. The luminance level of the holographic



Fig. 6. Holographic images acquired with various algorithms are photographed at the image plane of the display prototypes. From the left column, we provide the captured images of 8bit-SGD, 8bit-GS, B-SGD (TM=1), DOF-opt B-SGD ( $\gamma=0.01, TM=1$ ), B-SGD (TM=24), and DOF-opt B-SGD ( $\gamma=0.01, TM=24$ ) in focus and out of focus with 0.6 D difference. The PSNR estimated with the captured result of the focused image is provided in the bottom left corner of individual images, and the enlargements of the focused and defocused images are provided. The results are photographed with a gamma of 2.2. Notably, a certain amount of quality degradation occurs because of the color-unified band limitation and off-axis configuration of the display prototypes. The white balance of the images reconstructed with the 8-bit SLM is manipulated based on the 8bit-SGD images, resulting in undesirable color distortions in 8bit-GS images. Image sources from DIV2K dataset [Agustsson and Timofte, 2017].

stimulus was estimated as  $0.2 \text{ cd/m}^2$ , which is below the permissible level of laser exposure [on Non-Ionizing Radiation Protection et al., 1996]. We only performed experiments with a low luminance level because of potential eye safety issues in holographic displays. The luminance levels of three different displays were balanced by placing NDFs with different transmittance ratios in individual beam paths. Details on the apparatus can be found in the Supplementary Material.

**6.1.3 Procedure.** A subject viewed the 2-D stimulus presented 0.33 m (3 D) away with his/her left or right eye after adjusting the chin-and-head rest to properly place his/her eye at the eye-box of the display system. The subject was sequentially provided with a holographic image reconstructed with FLCoS SLM, an image reconstructed with LCoS SLM, and an image with an OLED panel, and each observance is verified. The experimental stimulus is a castle scene with a gray Maltese cross at the center. The target moved in depth sinusoidally from 0.2 m (5 D) to 1 m (1 D) and back over two periods with a unit duration of 20 s after a 5-s buffer for each trial. The overall range of motion is 4 D. Subsequently, we repeatedly measure the dynamic accommodation response thrice for each condition.

There were one reference mode and five different hologram modes: OLED in which micro-OLED displays the stimulus; 8bit-SGD, 8bit-GS in which LCoS SLM displays a single frame of 8bit hologram acquired with SGD and GS algorithms, respectively; B-SGD in which FLCoS SLM shows a binary hologram acquired with SGD algorithm; DOF-opt B-SGD ( $\gamma=0.01$  and  $\gamma=0.1$ ) in which FLCoS SLM displays a binary hologram optimized with the proposed algorithm. Additionally, the modes providing binary holograms were tested under various TM conditions: TM=1, 2, 4, 8, 16, 24. Thus, we evaluated 21 conditions, and there was 63 trials per subject. The conditions were randomly provided, and there was 30-s break between the trials. The tests were conducted over two separate days due to the excessive fatigue from a long-duration dynamic accommodation task because the experiment lasted approximately 1.5 hours.

**6.1.4 Data processing.** We acquired the measured data in the form of a comma-separated value (csv) file to analyze the data. We excluded the data corrupted by eye blinking, and subjected the response data to two periods, each of which has a duration of 20 s (1000 points) measured after a 5-second buffer at every trial. Six trials of each viewing condition are demonstrated in thin black lines as shown in Fig. 7(C). Each set of 1000 points was fitted to a sinusoid. Here, we fitted the measured data with a sinusoid at the target frequency with the amplitude, phase delay, and DC offset as free parameters with Levenberg-Marquardt damped least-squares method. We excluded the period when the valid measurement ratio was below 70 %, and the residual norm of curve-fitting is greater than 0.3. Furthermore, a fitted curve with the amplitude more than three standard deviations from the median amplitude was classified as an outlier and was excluded from the analysis. After the exclusions, we averaged the amplitudes for each condition.

Generally, the accommodative gain was estimated as the ratio of the amplitude of the fitted sinusoidal curve and the stimulus sinusoid [Koulieris et al., 2017]. However, we normalized accommodative gain with the mean amplitude of the fitted sinusoids with

data measured when viewing OLED because the highest observed accommodative gains measured under optimal conditions were saturated at a level of 0.8-0.9 [Kruger et al., 1993, MacKenzie et al., 2010] and accommodative gains highly vary between the subjects. The results from nine participants were excluded because of several reasons (5: lack of valid measurements due to small or large pupil (valid measurement ratio < 70 %), 2: low dioptric amplitude when viewing OLED (< 1.0 D), 1: misaligned stimuli depth, 1: different OLED gains within two separate days) and the exclusion was quite common in accommodation measurement experiments with untrained subjects [Padmanaban et al., 2017].

## 6.2 Results

We estimated the normalized accommodative gains of 21 subjects (14 female, mean age: 24.5, mean SE: -0.59 D) for each viewing condition and averaged across the subjects. The accommodation results are shown in Fig. 7(D, E). Figure 7(D) shows the normalized accommodative gains with a variable of TM frames, and Fig. 7(E) compares the accommodative gains measured when viewing holographic images provided by different single-frame CGHs.

There was a significant effect of speckle reduction on the improvement of accommodation response. The mean gains evaluated on B-SGD CGHs with different TM conditions (TM=1, 2, 4, 8, 16, 24) were 0.44, 0.61, 0.70, 0.76, 0.81, and 0.79, respectively. For DOF-opt B-SGD ( $\gamma=0.01$ ), the mean gains were measured as 0.53, 0.59, 0.71, 0.79, 0.73, and 0.77. Likewise, for DOF-opt B-SGD ( $\gamma=0.1$ ), those were 0.52, 0.58, 0.68, 0.74, 0.81, and 0.73. The nonparametric paired tests were conducted to support the statistical reliability of the experiments because the measured data failed to show normality with Shapiro-wilk test. One-tailed Wilcoxon tests yielded statistical significance on the measured gains of B-SGD pairs under consecutive TM conditions such as TM=1 versus TM=2 ( $p<0.001$ ), TM=2 versus TM=4 ( $p<0.05$ ), and TM=4 versus TM=8 ( $p<0.05$ ). The paired conditions of TM=8 versus TM=16 and TM=16 versus TM=24 did not show significant differences because the accommodative gain began to saturate. The mean normalized accommodative gains and speckle contrast ratio ( $C_s/C_o = 1/\sqrt{N}$  (in case of fully-developed speckle),  $C_o$ : speckle contrast at TM=1) showed a strong correlation with Pearson coefficient of -0.99 ( $p<0.001$ ). The absolute value of the speckle contrast at TM=1 varied depending on factors such as propagation distance from SLM, numerical aperture of the display system, pupil size, and coherence characteristics of light sources. The tests were conducted with scipy package in python.

Similarly, we conducted one-tailed Wilcoxon tests with the mean normalized gains measured when viewing holographic images of single-frame CGHs (8bit-SGD, 8bit-GS, B-SGD, DOF-opt B-SGD ( $\gamma=0.01$ ), DOF-opt B-SGD ( $\gamma=0.1$ )). They were estimated as 0.03, 0.46, 0.44, 0.53, and 0.52, respectively. There were strong statistical differences between the measured gains of 8bit-SGD CGHs and the other CGHs ( $p<0.001$ ). The CGHs acquired with the proposed algorithm (DOF-opt B-SGD ( $\gamma=0.01$  and  $\gamma=0.1$ )) showed significant improvements on accommodative gains over the case of primitive B-SGD under the condition of TM=1 (DOF-opt B-SGD ( $\gamma=0.01$ ) versus B-SGD:  $p<0.001$ , DOF-opt B-SGD ( $\gamma=0.1$ ) versus B-SGD:  $p<0.01$ ). DOF-opt B-SGD ( $\gamma=0.01$ ) showed a strong significant improvement

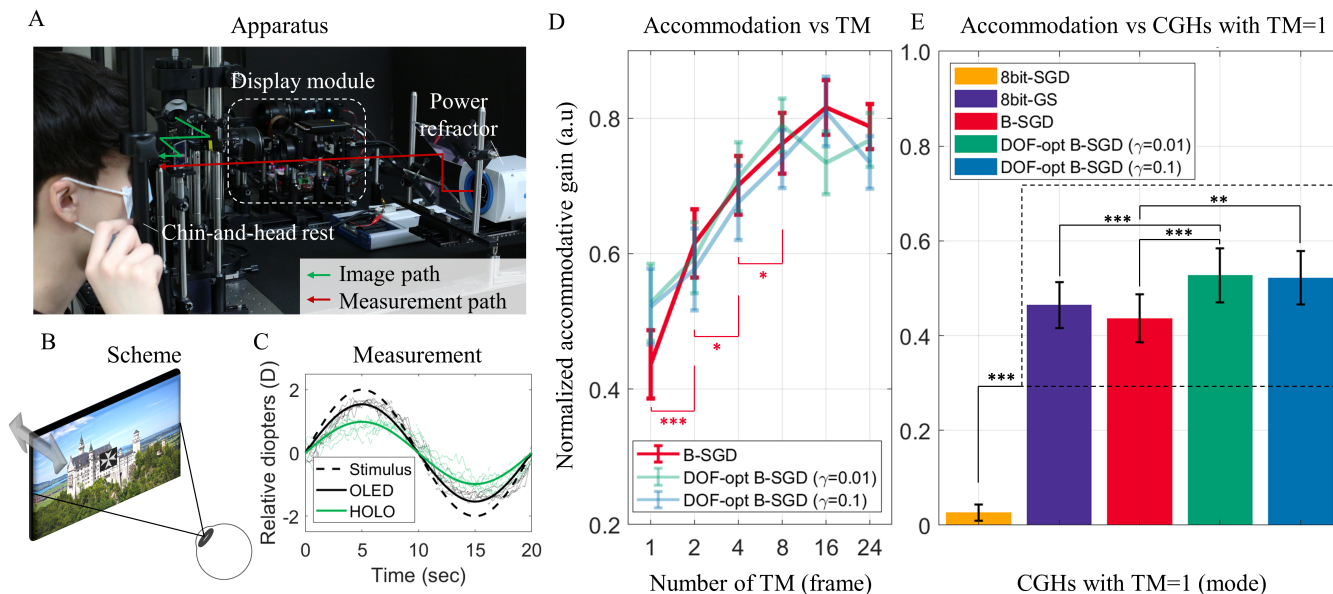


Fig. 7. Accommodation experiments. (A) Experimental apparatus constructed with display module (white dashed line) and accommodation measurement device. The participant views the stimulus (green arrow) with an eye, and the power refractor measures the refractive power of his/her eye (red arrow). During the test, the depth-varying stimulus; (B) a castle scene with a gray Maltese cross placed at the center, is provided. (C) The accommodative responses of an individual user are shown with representative instances measured when an incoherent display (OLED, black) or a holographic display (HOLO, green) presents a stimulus with dioptric modulation, as indicated by the dashed black line. The refractive powers, represented as thin lines, were measured six times for each subject, and fitted to a single sinusoid (solid lines). (D) The normalized accommodative gains, averaged across subjects, measured when viewing B-SGD CGH (red) and DOF-opt B-SGD CGHs ( $\gamma=0.01$ : green,  $\gamma=0.1$ : blue) with different TM conditions are provided. (E) The averages of the measured accommodative responses are compared when viewing holographic displays with CGHs under the condition of TM=1. Error bars indicate the standard error for each displaying mode. Asterisks indicate significant difference in the paired conditions as assessed by Wilcoxon rank sum test (\*:  $p<0.05$ , \*\*:  $p<0.01$ , \*\*\*:  $p<0.001$ ). These results show that speckle reduction through TM and the CGH optimization with additional regularization on contrast ratio effectively enhance the accommodative gain.

on normalized accommodation gain over 8bit-GS ( $p<0.001$ ), whereas the other modes of binary CGHs failed to show statistical significance (B-SGD versus 8bit-GS:  $p=0.82$ , DOF-opt B-SGD ( $\gamma=0.1$ ) versus 8bit-GS:  $p=0.056$ ). These results show the efficacy of the proposed CGH optimization algorithm.

Although the statistical tests were conducted on the pairs of binary holograms displayed in different TM conditions (TM=2, 4, 8, 16, 24), none of the tests yielded statistical significance. This may be because the proposed CGH acquisition targets a single hologram frame instead of a set of hologram frames utilized in TM. It can be resolved if the CGH acquisition algorithm is expanded to a multi-frame optimization [Curtis et al., 2021]. The measured accommodative gain of individual subjects for entire conditions are provided in the Supplementary Material.

In summary, speckle reduction through TM and the proposed CGH optimization strategy showed significant improvements in accommodative gains. However, the overall CGH acquisition time increases proportionally to the number of hologram frames utilized in TM. Similarly, the reconstructed holographic image acquired with the proposed algorithm sacrifices the quality of the focused image as shown in Fig. 4. We conduct user experiments evaluating the

subjective image quality of each CGH scheme to solve the potential concerns.

## 7 SUBJECTIVE IMAGE QUALITY ASSESSMENT

In this section, we perform subjective quality evaluations of holographic contents through pairwise comparisons to answer the following two questions: 1) which CGH algorithm delivers a high-quality image in the actual holographic viewing experience? 2) does the holographic image realized by the proposed algorithm contain noticeable artifacts?

### 7.1 Methods

**7.1.1 Subjects.** The subjects who participated in the accommodation experiments participated in the experiments. The previous experiments were separately performed in two days. Therefore, the experiments were conducted in the remaining time after the accommodation experiments. Three of the thirty participants who completed the accommodation experiment could not complete the experiments in part because of a lack of time.

**7.1.2 Apparatus.** The identical apparatus was utilized as in the accommodation experiments without accommodation measurement.

**7.1.3 Procedure.** Figure 8 presents an overview of subjective image quality evaluation experiments. Figure 8(A) shows the experimental scheme of subjective image quality evaluation performed with two-interval forced choice (2-IFC) method [Bogacz et al., 2006]. The subject sequentially views a pair of holographic images presented 0.33 m (3 D) away for 1.5 s per each image, and a blank screen was provided for 0.5 s between the images. Subsequently, the subject is asked to select a ‘high-contrast and less-noisy’ image with the keypad with no tie options shown in Fig. 8(B). It is reported that ‘no preference’ option can underestimate the difference [Perez-Ortiz and Mantiuk, 2017]. Before the experiments, each subject viewed the stimuli provided by the OLED panel as reference images. Additionally, the sequence of two options in the 2-IFC experiments was randomly shuffled to prevent a decision bias to either former or latter option.

Because the entire number of conditions was 20 (8bit-SGD, 8bit-GS, B-SGD (TM=1, 2, 4, 8, 16, 24), DOF-opt B-SGD ( $\gamma=0.01, 0.1/TM=1, 2, 4, 8, 16, 24$ )), the complete pairwise comparisons could not be performed. Thus, we separated the full-scale experiment into two. The first experiment was performed with conventional CGHs (8bit-SGD, 8bit-GS, and B-SGD (TM=1, 2, 4, 8, 16, 24)) which results in 8 options and 28 pairs. For every pair, three trials were performed. Thus, the first experiment comprised 84 trials per stimulus. Three-minute break was given between each session. For second experiment, we partially compared the holographic images realized by binary holograms with identical TM conditions. The experiments were performed in six different TM conditions with three pairs of binary holograms and three trials per each pair. Thus, the second experiment consisted of 54 trials per stimulus. The pairwise comparisons of various CGH algorithms with three different stimuli consisted of 414 trials, which also took approximately 1.5 h to finish the entire task. Additional information on the procedure is provided in the Supplementary Material.

## 7.2 Results

The results of the subjective image quality evaluation of holographic contents (8bit-SGD, 8bit-GS, B-SGD with TM=1, 2, 4, 8, 16, 24) based on pairwise comparisons were scaled under Thurston model V [Perez-Ortiz and Mantiuk, 2017] and the matrices with accumulated vote counts were converted to a JOD unit [Mantiuk et al., 2011, 2021] as shown in Figure 8(C). Comparison matrices of three stimuli were summed up to a single matrix. The responses from one subject were excluded because the subject was classified as an outlier based on the outlier analysis introduced by Perez-Ortiz and Mantiuk [2017]. The subject’s responses showed an inter-quartile-normalized score of 6.59, which is above the customary threshold of 1.5. Thus, we subjected the data from 27 subjects (2: incomplete, 1: outlier) and the total number of accumulated vote counts was 6,804. The JOD values were regularized to present a mean JOD value of zero. The holographic contents demonstrated JOD of 0.02, -2.17, -1.39, -0.55, 0.26, 1.05, 1.34, and 1.43. There was a difference of approximately 0.8 JOD as the number of TM frames doubled (speckle noise reduced in a ratio of square root of two) until it reached eight, representing a preference of about 40% over the paired option. However, the JOD

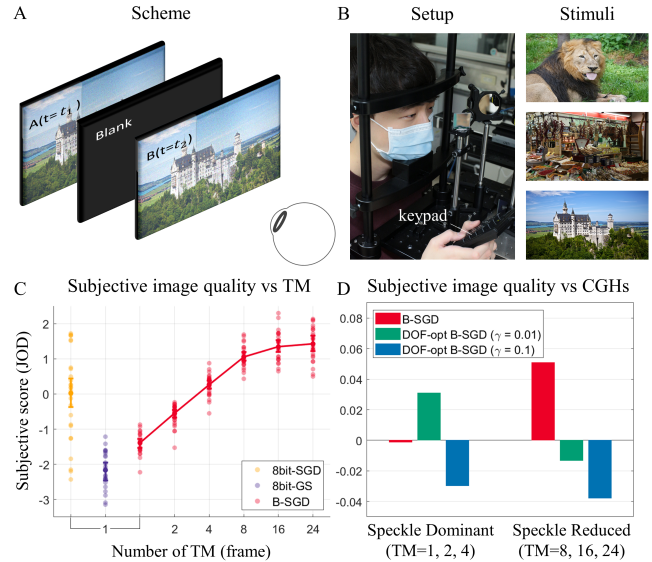


Fig. 8. Subjective image quality evaluation on holographic contents through pairwise comparisons. (A) Illustration of the experimental scheme that summarizes the 2-IFC experiments. (B) In the experiments, the user chooses the preferable option with the keypad and the entire experiments are performed with three different stimuli (lion, market, and castle scenes) from DIV2K dataset [Agustsson and Timofte, 2017]. (C) Pairwise comparisons when viewing a holographic near-eye display with various CGHs (8bit-SGD: yellow, 8bit-GS: purple, B-SGD: red) are performed and the responses are scaled in a linear unit of JOD (just objectionable difference). Each point represents the JOD of each scheme derived from the responses of individual users. The difference of 1 JOD corresponds to 50% preference of the option over the other option. Error bars represent 95% confidence intervals estimated using bootstrapping. (D) Pairwise comparisons of the binary holograms (B-SGD, DOF-opt B-SGD ( $\gamma=0.01$ ), and DOF-opt B-SGD ( $\gamma=0.1$ )) are performed and the user responses are scaled in unit of JOD. The results are categorized into two conditions depending on the level of speckle reduction; *Speckle Dominant* (TM=1, 2, 4) and *Speckle Reduced* (TM=8, 16, 24).

difference between B-SGD (TM=8) and B-SGD (TM=16) noticeably decreased to 0.3, corresponding to 16% of preference probability.

Unlike the PSNR evaluations with the captured images as provided in Fig. 6 and Fig. S2-S4, the 8bit-SGD holographic images exhibited relatively low JOD average with significantly large deviations. The potential cause of the unexpected degradation in subjective image quality of the 8bit-SGD case may root from the lack of tolerance to the artifacts such as scratches or dirt that may undesirably exist in the optical system. Camera-in-the-loop calibration [Chakravarthula et al., 2020, Peng et al., 2020] may solve this problem; however, it is limited to the artifacts present in the display system. Some subjects reported moving particles with ringing patterns in color on 8bit-SGD images. The dust or debris present in the tear film of user’s eye may cause this type of defects in the image as the proportional coherent beam is localized in a small section of the pupil in case of 8bit-SGD images. The tolerance of each CGH to the artifacts inevitably present in the pupil plane and the image plane is tested, and the captured results are provided in the Supplementary

Material. The results show that 8bit-SGD images are susceptible to the artifacts. Moreover, the noticeable JOD difference between 8bit-GS and B-SGD TM=1 may result from the undesirable color distortions in 8bit-GS images as shown in Fig. 6.

We compared the binary holograms acquired with different algorithms (B-SGD, DOF-opt B-SGD ( $\gamma=0.01$ , and  $\gamma=0.1$ )) as shown in Fig. 8(D). The total number of trials was insufficient to derive the result if the results are individually sorted based on image and TM conditions. Thus, we classified the cases of binary holograms reconstructed with TM=1, 2, 4 conditions, and TM=8, 16, 24 conditions and named them as *Speckle Dominant* and *Speckle Reduced*. The vote counts of 28 subjects (1: incomplete, 1: outlier) corresponding to each category are combined to derive JOD values. In the case of *Speckle Dominant*, the participants could not distinguish speckle noise and the noise from additional regularization since the JOD is estimated 0, 0.031, and -0.030, for B-SGD, DOF-opt B-SGD ( $\gamma=0.01$ ), and DOF-opt B-SGD ( $\gamma=0.1$ ), respectively. Conversely, in the case of *Speckle Reduced*, the subjects began distinguishing the artificial noise since the measured JOD is 0.051, -0.013, and -0.038 for B-SGD, DOF-opt B-SGD ( $\gamma=0.01$ ), and DOF-opt B-SGD ( $\gamma=0.1$ ), respectively. Furthermore, large weights on the  $l_1$  regularization term in the optimization process can lead to noticeable image quality degradation since DOF-opt B-SGD ( $\gamma=0.1$ ) was ranked last among the three candidates. Thus, the proposed CGH algorithm delivers holographic images that can be hardly distinguished from the image provided by the primitive method when the speckle is dominantly present.

## 8 DISCUSSION

In summary, we assessed the holographic contents acquired with various CGH algorithms based on accommodative gain and subjective image quality. The evaluations with the prototype of holographic near-eye displays confirmed that the adequate bandwidth size of holographic contents should be guaranteed to provide holographic stimuli with monocular accommodation cues. In a holographic viewing environment with a sufficiently wide eye-box as our prototype, speckle reduction significantly improves the accommodative gain. Moreover, the proposed CGH optimization algorithm with regularization on contrast ratio demonstrated significance in the measured accommodative gains as it ranked first among the tested single-frame CGHs and showed indistinguishable quality degradation compared among the binary holograms.

### 8.1 Limitations and Future Works

**8.1.1 Model mismatch by human eye.** In this study, CGH optimization was performed assuming a diffraction-limited eye with fixed pupil diameter. However, in reality, the subjects' pupils were repeatedly dilated and contracted over time, ranging their sizes from 4-8 mm even in the uniform luminance setting. In addition, eye aberrations were present even in a normal eye, specifically exaggerated in a large pupil condition. This discrepancy in the simulated and actual experimental conditions may have limited the validation of this study. Chakravarthula et al. [2021] introduced the speckle reduction in holographic displays by providing the optimized CGH based on a target optical model of one's eye. While this approach is plausible, it is hardly applicable at the current level of technology

as the speckle reappears even with a minute model mismatch that is inevitably present.

**8.1.2 Experimental apparatus.** The evaluations were performed in a single viewing condition of the field of view and eye-box of display prototype and a single luminance level of visual stimuli. When the near-eye display offers a wide field of view image with a small eye-box, the retinal disparity may become a primary factor to drive accommodation response [Del Águila-Carrasco et al., 2017] unlike the prototype used in this study. The average size of the speckle may be enlarged, and the spatial frequency region corresponding to the speckle noise may shift to a lower range. Moreover, people are less sensitive to the noise in a higher luminance level since the light sensitivity maximizes in the scotopic (dark-adapted) state. Nevertheless, the user evaluations can hardly be approved due to potential eye safety issues on laser light sources. Evaluation of holographic contents in various viewing conditions can establish a visual threshold for speckle noise present in holographic displays and further enrich the visual experience through holographic displays.

**8.1.3 CGH rendering speed.** The hologram acquisition time is relatively long as it reconstructs the images of the sampled focal states to estimate the contrast ratio of the reconstructed hologram. In this work, we mainly focused on the user evaluation of holographic contents, although real-time CGH rendering is key for advanced holographic displays. The CGH acquisition speed can be improved in the near future as recent works have begun to generate holograms in real-time frame rates with deep learning technology [Horisaki et al., 2018, Lee et al., 2020a, Peng et al., 2020, Shi et al., 2021].

**8.1.4 Holographic contents.** The evaluations were performed based on 2-D holographic contents, although the high-quality holographic realization of 3-D scenes was recently introduced [Choi et al., 2021, Lee et al., 2022, Shi et al., 2021]. The primary reason for the scope limitation was that the quantitative criteria on evaluation of autostereoscopic 3-D displays, especially holographic display, are still vague and evaluations on 3-D contents are often carried with questionnaire-based subjective evaluations [Hoffman et al., 2008].

**8.1.5 Speckle reduction with other approaches.** We adopted the temporal multiplexing technique as a means to reduce speckle without spatial and angular resolution loss. Similarly, additional physical factors are required for robust speckle reduction in holographic displays, and the employment of partially coherent sources is an alternative solution that can be adopted in limited frame rates condition. However, determining the acceptable resolution loss due to partial coherence of light sources remains an open question, and investigation through user experiments will be an interesting topic for the relevant community.

## 9 CONCLUSION

For next-generation virtual reality and augmented reality applications, support of accommodation cue is crucial for a perceptually realistic viewing experience. We studied the potential factors that limit the accommodation response in the emerging holographic near-eye display, introduced approaches to improve the response,

and validated the efficacy of the approaches with experimental assessments including several user studies. With this study focusing on the speckle phenomenon, a unique characteristic inherently present in holographic displays with coherent sources establishes a guideline on user evaluations with holographic displays and contributes to the diversity of evaluation metrics on holographic contents.

## ACKNOWLEDGMENTS

This work is supported by the Institute for Information and Communications Technology Promotion Grant funded by the Korea Government (MSIT) (development of vision assistant HMD and contents for the legally blind and low vision) (No. 2017-0-00787).

## REFERENCES

- Eirikur Agustsson and Radu Timofte. 2017. Ntire 2017 challenge on single image super-resolution: Dataset and study. In *Proceedings of the IEEE conference on computer vision and pattern recognition workshops*. 126–135.
- Kurt Akeley, Simon J. Watt, Ahna Reza Girshick, and Martin S. Banks. 2004. A Stereo Display Prototype with Multiple Focal Distances. *ACM Trans. Graph.* 23, 3 (2004), 804–813.
- Martin S Banks, Wilson S Geisler, and Patrick J Bennett. 1987. The physical limits of grating visibility. *Vision research* 27, 11 (1987), 1915–1924.
- Peter GJ Barten. 1999. *Contrast sensitivity of the human eye and its effects on image quality*. SPIE press.
- Stephen A Benton and V Michael Bove Jr. 2008. *Holographic imaging*. John Wiley & Sons.
- Rafal Bogacz, Eric Brown, Jeff Moehlis, Philip Holmes, and Jonathan D Cohen. 2006. The physics of optimal decision making: a formal analysis of models of performance in two-alternative forced-choice tasks. *Psychological Review* 113, 4 (2006), 700.
- SE Broomfield, MAA Neil, EGS Paige, and GG Yang. 1992. Programmable binary phase-only optical device based on ferroelectric liquid crystal SLM. *Electronics Letters* 28, 1 (1992), 26–28.
- Praneeth Chakravarthula, Yifan Peng, Joel Kollin, Henry Fuchs, and Felix Heide. 2019. Wirtinger Holography for Near-Eye Displays. 38, 6, Article 213 (2019), 13 pages.
- Praneeth Chakravarthula, Ethan Tseng, Tarun Srivastava, Henry Fuchs, and Felix Heide. 2020. Learned Hardware-in-the-Loop Phase Retrieval for Holographic near-Eye Displays. *ACM Trans. Graph.* 39, 6, Article 186 (2020), 18 pages.
- Praneeth Chakravarthula, Zhan Zhang, Okan Tursun, Piotr Didyk, Qi Sun, and Henry Fuchs. 2021. Gaze-contingent retinal speckle suppression for perceptually-matched foveated holographic displays. *IEEE Transactions on Visualization and Computer Graphics* 27, 11 (2021), 4194–4203.
- Chenliang Chang, Kiseung Bang, Gordon Wetzstein, Byoung-ho Lee, and Liang Gao. 2020. Toward the next-generation VR/AR optics: a review of holographic near-eye displays from a human-centric perspective. *Optica* 7, 11 (2020), 1563–1578.
- Suyeon Choi, Manu Gopakumar, Yifan Peng, Jonghyun Kim, and Gordon Wetzstein. 2021. Neural 3D Holography: Learning Accurate Wave Propagation Models for 3D Holographic Virtual and Augmented Reality Displays. *ACM Trans. Graph.* 40, 6, Article 240 (2021), 12 pages.
- Steven A. Cholewiak, Gordon D. Love, Pratul P. Srinivasan, Ren Ng, and Martin S. Banks. 2017. Chromablur: Rendering Chromatic Eye Aberration Improves Accommodation and Realism. *ACM Trans. Graph.* 36, 6, Article 210 (2017), 12 pages.
- Bruce G Cumming and Stuart J Judge. 1986. Disparity-induced and blur-induced convergence eye movement and accommodation in the monkey. *Journal of Neurophysiology* 55, 5 (1986), 896–914.
- Vincent R Curtis, Nicholas W Cairra, Jiayi Xu, Asha Gowda Sata, and Nicolas C Pégard. 2021. DCGH: Dynamic computer generated holography for speckle-free, high fidelity 3D displays. In *2021 IEEE Virtual Reality and 3D User Interfaces (VR)*. IEEE, 1–9.
- Scott J Daly. 1992. Visible differences predictor: an algorithm for the assessment of image fidelity. In *Human Vision, Visual Processing, and Digital Display III*, Vol. 1666. International Society for Optics and Photonics, 2–15.
- Antonio J Del Águila-Carrasco, Iván Marín-Franch, Paula Bernal-Molina, José J Esteve-Taboada, Philip B Kruger, Robert Montés-Micó, and Norberto López-Gil. 2017. Accommodation responds to optical vergence and not defocus blur alone. *Investigative ophthalmology & visual science* 58, 3 (2017), 1758–1763.
- Yuanbo Deng and Daping Chu. 2017. Coherence properties of different light sources and their effect on the image sharpness and speckle of holographic displays. *Scientific Reports* 7, 1 (2017), 1–12.
- James R Fienup. 1982. Phase retrieval algorithms: a comparison. *Applied Optics* 21, 15 (1982), 2758–2769.
- Edgar F Fincham. 1951. The accommodation reflex and its stimulus. *The British Journal of Ophthalmology* 35, 7 (1951), 381.
- Ralph W Gerchberg. 1972. A practical algorithm for the determination of phase from image and diffraction plane pictures. *Optik* 35 (1972), 237–246.
- Joseph W Goodman. 2005. *Introduction to Fourier optics*. Roberts and Company Publishers.
- Joseph W Goodman. 2007. *Speckle phenomena in optics: theory and applications*. Roberts and Company Publishers.
- Brian Guenter, Mark Finch, Steven Drucker, Desney Tan, and John Snyder. 2012. Foveated 3D graphics. *ACM Transactions on Graphics (TOG)* 31, 6 (2012), 1–10.
- David M Hoffman, Ahna R Girshick, Kurt Akeley, and Martin S Banks. 2008. Vergence-accommodation conflicts hinder visual performance and cause visual fatigue. *Journal of Vision* 8, 3 (2008), 33–33.
- Ryoichi Horisaki, Ryoosuke Takagi, and Jun Tanida. 2018. Deep-learning-generated holography. *Applied Optics* 57, 14 (2018), 3859–3863.
- Chung-Kai Hsueh and Alexander A Sawchuk. 1978. Computer-generated double-phase holograms. *Applied Optics* 17, 24 (1978), 3874–3883.
- Fu-Chung Huang, David P Luebke, and Gordon Wetzstein. 2015. The light field stereoscope. In *SIGGRAPH emerging technologies*. 24–1.
- Changwon Jang, Kiseung Bang, Gang Li, and Byoung-ho Lee. 2018. Holographic Near-Eye Display with Expanded Eye-Box. *ACM Trans. Graph.* 37, 6, Article 195 (dec 2018), 14 pages.
- Changwon Jang, Kiseung Bang, Seokil Moon, Jonghyun Kim, Seungjae Lee, and Byoung-ho Lee. 2017. Retinal 3D: Augmented Reality near-Eye Display via Pupil-Tracked Light Field Projection on Retina. *ACM Trans. Graph.* 36, 6, Article 190 (2017), 13 pages.
- Donald H Kelly. 1979. Motion and vision. II. Stabilized spatio-temporal threshold surface. *Josa* 69, 10 (1979), 1340–1349.
- Dongyeon Kim, Seung-Woo Nam, Kiseung Bang, Byoung-hyo Lee, Seungjae Lee, Youngmo Jeong, Jong-Mo Seo, and Byoung-ho Lee. 2021. Vision-correcting holographic display: evaluation of aberration correcting hologram. *Biomedical Optics Express* 12, 8 (2021), 5179–5195.
- Robert Konrad, Nitish Padmanaban, Keenan Molner, Emily A. Cooper, and Gordon Wetzstein. 2017. Accommodation-Invariant Computational near-Eye Displays. *ACM Trans. Graph.* 36, 4, Article 88 (2017), 12 pages.
- George-Alex Koulieris, Bee Bui, Martin S. Banks, and George Drettakis. 2017. Accommodation and Comfort in Head-Mounted Displays. *ACM Trans. Graph.* 36, 4, Article 87 (2017), 11 pages.
- Brooke Krajancich, Petr Kellnhofer, and Gordon Wetzstein. 2021. A Perceptual Model for Eccentricity-dependent Spatio-temporal Flicker Fusion and its Applications to Foveated Graphics. *ACM Trans. Graph.* 40 (2021), Issue 4.
- Philip B Kruger, Steven Mathews, Karan R Aggarwala, and Nivian Sanchez. 1993. Chromatic aberration and ocular focus: Fincham revisited. *Vision Research* 33, 10 (1993), 1397–1411.
- Grace Kuo, Laura Waller, Ren Ng, and Andrew Maimone. 2020. High Resolution eTendue Expansion for Holographic Displays. *ACM Trans. Graph.* 39, 4, Article 66 (2020), 14 pages.
- Byoung-ho Lee, Dongyeon Kim, Seungjae Lee, Chun Chen, and Byoung-ho Lee. 2022. High-contrast, speckle-free, true 3D holography via binary CGH optimization. *Scientific Reports* 12, 1 (18 Feb 2022), 2811. <https://doi.org/10.1038/s41598-022-06405-2>
- Byoung-ho Lee, Dongheon Yoo, Jinsoo Jeong, Seungjae Lee, Dukho Lee, and Byoung-ho Lee. 2020c. Wide-angle speckleless DMD holographic display using structured illumination with temporal multiplexing. *Optics Letters* 45, 8 (2020), 2148–2151.
- Juhyun Lee, Jinsoo Jeong, Jaebum Cho, Dongheon Yoo, Byoung-ho Lee, and Byoung-ho Lee. 2020a. Deep neural network for multi-depth hologram generation and its training strategy. *Optics Express* 28, 18 (2020), 27137–27154.
- Seungjae Lee, Youngjin Jo, Dongheon Yoo, Jaebum Cho, Dukho Lee, and Byoung-ho Lee. 2019. Tomographic near-eye displays. *Nature communications* 10, 1 (2019), 1–10.
- Seungjae Lee, Dongyeon Kim, Seung-Woo Nam, Byoung-ho Lee, Jaebum Cho, and Byoung-ho Lee. 2020b. Light source optimization for partially coherent holographic displays with consideration of speckle contrast, resolution, and depth of field. *Scientific Reports* 10, 1 (2020), 1–12.
- Wai Hon Lee. 1970. Sampled Fourier transform hologram generated by computer. *Applied Optics* 9, 3 (1970), 639–643.
- Gang Li, Dukho Lee, Youngmo Jeong, Jaebum Cho, and Byoung-ho Lee. 2016. Holographic display for see-through augmented reality using mirror-lens holographic optical element. *Optics Letters* 41, 11 (2016), 2486–2489.
- Yongjun Lim, Keehoon Hong, Hwi Kim, Hyun-Eui Kim, Eun-Young Chang, Soohyun Lee, Taone Kim, Jeho Nam, Hyon-Gon Choo, Jinwoong Kim, et al. 2016. 360-degree tabletop electronic holographic display. *Optics Express* 24, 22 (2016), 24999–25009.
- Kevin J MacKenzie, David M Hoffman, and Simon J Watt. 2010. Accommodation to multiple-focal-plane displays: Implications for improving stereoscopic displays and for accommodation control. *Journal of Vision* 10, 8 (2010), 22–22.
- Andrew Maimone, Andreas Georgiou, and Joel S Kollin. 2017. Holographic near-eye displays for virtual and augmented reality. *ACM Transactions on Graphics (TOG)* 36, 4 (2017), 1–16.

- Rafal Mantiuk, Kil Joong Kim, Allan G. Rempel, and Wolfgang Heidrich. 2011. HDR-VDP-2: A Calibrated Visual Metric for Visibility and Quality Predictions in All Luminance Conditions. *ACM Trans. Graph.* 30, 4, Article 40 (2011), 14 pages.
- Rafal K. Mantiuk, Gyorgy Denes, Alexandre Chapiro, Anton Kaplanyan, Gizem Rufo, Romain Bachy, Trisha Lian, and Anjul Patney. 2021. FovVideoVDP: A Visible Difference Predictor for Wide Field-of-View Video. *ACM Trans. Graph.* 40, 4, Article 49 (2021), 19 pages.
- Theodore G Martens and Kenneth N Ogle. 1959. Observations on accommodative convergence: Especially its nonlinear relationships. *American Journal of Ophthalmology* 47, 1 (1959), 455–463.
- Steven Mathews and Philip B Kruger. 1994. Spatiotemporal transfer function of human accommodation. *Vision Research* 34, 15 (1994), 1965–1980.
- Arian Mehrfard, Javad Fotouhi, Giacomo Taylor, Tess Forster, Nassir Navab, and Bernhard Fuerst. 2019. A comparative analysis of virtual reality head-mounted display systems. *arXiv preprint arXiv:1912.02913* (2019).
- Rafael Navarro, Pablo Artal, and David R Williams. 1993. Modulation transfer of the human eye as a function of retinal eccentricity. *JOSA A* 10, 2 (1993), 201–212.
- Aya Nozaki, Masaya Mitobe, Fumio Okuyama, and Yuji Sakamoto. 2017. Dynamic visual responses of accommodation and vergence to electro-holographic images. *Optics Express* 25, 4 (2017), 4542–4551.
- Ryuichi Ohara, Masanobu Kurita, Takuo Yoneyama, Fumio Okuyama, and Yuji Sakamoto. 2015. Response of accommodation and vergence to electro-holographic images. *Applied Optics* 54, 4 (2015), 615–621.
- International Commission on Non-Ionizing Radiation Protection et al. 1996. Guidelines on limits of exposure to laser radiation of wavelengths between 180 nm and 1,000  $\mu\text{m}$ . *Health Physics* 71, 5 (1996), 804–819.
- DA Owens. 1980. A comparison of accommodative responsiveness and contrast sensitivity for sinusoidal gratings. *Vision Research* 20, 2 (1980), 159–167.
- Nitish Padmanaban, Robert Konrad, Tal Stramer, Emily A Cooper, and Gordon Wetzstein. 2017. Optimizing virtual reality for all users through gaze-contingent and adaptive focus displays. *Proceedings of the National Academy of Sciences* 114, 9 (2017), 2183–2188.
- Jongchan Park, KyeoReh Lee, and YongKeun Park. 2019. Ultrathin wide-angle large-area digital 3D holographic display using a non-periodic photon sieve. *Nature Communications* 10, 1 (2019), 1–8.
- Yifan Peng, Suyeon Choi, Jonghyun Kim, and Gordon Wetzstein. 2021. Speckle-free holography with partially coherent light sources and camera-in-the-loop calibration. *Science Advances* 7, 46 (2021), eabg5040.
- Yifan Peng, Suyeon Choi, Nitish Padmanaban, and Gordon Wetzstein. 2020. Neural Holography with Camera-in-the-Loop Training. *ACM Trans. Graph.* 39, 6, Article 185 (nov 2020), 14 pages.
- Maria Perez-Ortiz and Rafal K Mantiuk. 2017. A practical guide and software for analysing pairwise comparison experiments. *arXiv preprint arXiv:1712.03686* (2017).
- Sowmya Ravikumar, Kurt Akeley, and Martin S Banks. 2011. Creating effective focus cues in multi-plane 3D displays. *Optics Express* 19, 21 (2011), 20940–20952.
- Stephan Reichelt, Ralf Häussler, Gerald Fütterer, and Norbert Leister. 2010. Depth cues in human visual perception and their realization in 3D displays. In *Three-Dimensional Imaging, Visualization, and Display 2010 and Display Technologies and Applications for Defense, Security, and Avionics IV*, Vol. 7690. International Society for Optics and Photonics, 76900B.
- Liang Shi, Beichen Li, Changil Kim, Petr Kellnhofer, and Wojciech Matusik. 2021. Towards real-time photorealistic 3D holography with deep neural networks. *Nature* 591, 7849 (2021), 234–239.
- Yasuhiro Takaki and Naoya Okada. 2009. Hologram generation by horizontal scanning of a high-speed spatial light modulator. *Applied Optics* 48, 17 (2009), 3255–3260.
- Yasuhiro Takaki and Masahito Yokouchi. 2012. Accommodation measurements of horizontally scanning holographic display. *Optics Express* 20, 4 (2012), 3918–3931.
- Larry N Thibos, Xin Hong, Arthur Bradley, and Xu Cheng. 2002. Statistical variation of aberration structure and image quality in a normal population of healthy eyes. *JOSA A* 19, 12 (2002), 2329–2348.
- Christopher W Tyler and Russell D Hamer. 1990. Analysis of visual modulation sensitivity. IV. Validity of the Ferry–Porter law. *JOSA A* 7, 4 (1990), 743–758.
- Koki Wakunami, Po-Yuan Hsieh, Ryutaro Oi, Takanori Senoh, Hisayuki Sasaki, Yasuyuki Ichihashi, Makoto Okui, Yi-Pai Huang, and Kenji Yamamoto. 2016. Projection-type see-through holographic three-dimensional display. *Nature Communications* 7, 1 (2016), 1–7.
- Andrew B Watson. 2013. A formula for the mean human optical modulation transfer function as a function of pupil size. *Journal of Vision* 13, 6 (2013), 18–18.
- Gordon Wetzstein, Douglas R Lanman, Matthew Waggener Hirsch, and Ramesh Raskar. 2012. Tensor displays: compressive light field synthesis using multilayer displays with directional backlighting. (2012).
- Han-Ju Yeom, Hee-Jae Kim, Seong-Bok Kim, HuiJun Zhang, BoNi Li, Yeong-Min Ji, Sang-Hoo Kim, and Jae-Hyeung Park. 2015. 3D holographic head mounted display using holographic optical elements with astigmatism aberration compensation. *Optics Express* 23, 25 (2015), 32025–32034.